Scale characterisation of an oxidised (Hf,Ti)C-SiC ultra-high temperature ceramic matrix composite

Makurunje, Phylis; Sigalas, Iakovos; Binner, Jon

DOI:
10.1016/j.jeurceramsoc.2020.08.048

Document Version
Peer reviewed version

Citation for published version (Harvard):
Makurunje, P, Sigalas, I & Binner, J 2021, 'Scale characterisation of an oxidised (Hf,Ti)C-SiC ultra-high temperature ceramic matrix composite', *Journal of the European Ceramic Society*, vol. 41, no. 1, pp. 167-175. https://doi.org/10.1016/j.jeurceramsoc.2020.08.048

Characterisation of an oxidised SiC-TiC-HfC ultra-high temperature ceramic matrix composite scale

Phylis Makurunje[1, 2*], Iakovos Sigalas[1, 2], Jon Binner[3]

[1] DST-NRF Centre of Excellence in Strong Materials, University of the Witwatersrand, Johannesburg, South Africa

[2] School of Chemical and Metallurgical Engineering, University of the Witwatersrand, Johannesburg, South Africa

[3] School of Metallurgy & Materials, University of Birmingham, Birmingham, UK

[*]Corresponding author:

Tel: +27 11 717 7502; Fax: +27 11 7176XBB; e-mail: phylis.makurunje@wits.ac.za pmakurunje@gmail.com

Abstract

A hybrid carbide ultra-high temperature ceramics matrix [(Hf,Ti)C-SiC] reinforced with BN-coated carbon fibres was fabricated and tested for surface oxidation resistance. The UHTC composite showed an average mass ablation rate of 0.0014 g/s after exposure to a high heat flux (~17 MW/cm^2) oxyacetylene flame test for 30 s. The cross-sectional profile of the oxides scale formed was characterised and analysed. The scale was multicomponent; consisting of oxides of Hf, Ti and Si, as well as $HfTiO_4$ and $HfSiO_4$, which underwent phase separation and immiscibility. Multiple glassy bubbles formed on the scale surface due to the impediment of escaping gases by the glassy layer on the outer scale. The largest pores in the scale and surface bubbles that resisted rupture were the dominant features of the outermost phase-separated layer. Phase separation in the scale top layer improves the resistance to scale rupture.

Key Words

Ceramic matrix composite, UHTC, phase immiscibility, oxyacetylene torch, oxidation scale

1. Introduction

The advent of hypersonic flight demands the use of very refractory materials for applications such as thermal protection systems (TPS)[1,2]. One group of materials that is widely investigated is ultra-high temperature ceramics (UHTCs). The need to have materials that have resilience to oxidative attack, while retaining mechanical properties at temperatures above 2000 °C is desirable. Oxidation at such temperatures may be regarded as inevitable; therefore the ability of such materials to oxidise minimally and form an oxidative scale that firmly adheres to the virgin material becomes a key criterion[3].

Most UHTC materials have SiC added to Zr- and Hf-based UHTC compounds for better sintering and oxidation resistance, leading to a multi-graded or multi-layered scale when oxidised. The profiles of the multi-layer oxide scale that forms on ZrB_2-SiC compounds have been explained in detail[4–6], whilst oxidised HfB_2-SiC refractory compounds scales have also been reported in the literature[7–9]. Mechanisms of scale profile formation in UHTCs incorporating both Zr- and Hf-UHTCs show similar trends to the primary compounds[4,8]. Additions to the Zr- and Hf-based refractory compounds have also been made using Group V and Group VI compounds. The contribution of the former to modifying Zr and/or Hf scales, particularly using Ta compounds like TaC, TaB_2 and $TaSi_2$ for better oxidation resistance and sintering, have been investigated[6,10,11], whilst additions of Group VI compounds, especially WC, WB_2 and WSi_2 to improve sintering and sealing of voids in Zr- and/or Hf-based scales have also been investigated[12–14]. Notwithstanding the various incorporations to Zr and Hf, the widely accepted scale profile, from the scale/virgin material interface to the surface, consists of a silica-depleted layer that leads to a glassy silica-rich layer on the outside of the scale.

Of interest are situations where phase separation occurs in some or all layers of the UHTC oxide scale profile formed. Immiscibility in UHTC systems has mostly been studied in Zr-based systems. Phase separation occurred on the outer surface in a ZrB_2-20% SiC system with 20% $TaSi_2$ additions[6], whilst ZrO_2 particles crystallised out of a silicate matrix in a ZrB_2-20% SiC system with rare earth additives such as LaB_6, La_2O_3 and Gd_2O_3[15]. Phase separation also occurred between ZrO_2 and SiO_2 on the surface of a ZrB_2–15 vol% SiC composite[16] and in a ZrB_2-Si_3N_4 UHTC with TaB_2 and CrB_2 additions[10]. For the latter, the borosilicate glass formed separated from the oxides of Zr and Cr[10]. Verdon and co-workers[17] were probably the first to show how phase separation could be useful in oxidation protection of a HfO_2-SiO_2 system generated from a HfC-SiC coating on a C/C composite. Makurunje et al.[18] showed phase separation in the form of incipient crystallization and surface bubbles in a system consisting of Ta_2O_5, SiO_2 and TiO_2.

From consideration of the contribution of cationic electric fields and size contribution to phase immiscibility[19–21], when a silicon-rich hybrid-matrix UHTC is oxidised, phase separation should occur. Some studies also showed that the presence of cations such as Ta^{x+} and Cr^{y+} in hybrid-matrix UHTCs could initiate phase separation[10]. A hybrid-matrix UHTC can be considered as one consisting of at least two transition metal compounds that are considered UHTCs, often also containing SiC. Phase separation in hybrid-matrix UHTCs can be associated with Coulombic separations between the electric fields around the cations. The case of SiC being oxidised to polymerized silica leads to the oxygen anions being closer to the silica network, which causes the transition metal cations' fields to repel, hence generating phase separation.

The present work consists of an investigation into the scale profile and surface of a carbon fibre reinforced hybrid carbide UHTC matrix, the latter consisting of a combination of SiC and (Ti,Hf)C. The combination of TiC and HfC in a UHTC composite matrix has not been investigated previously. The occurrence of oxides immiscibility and its effect on protecting the underlying carbide composite is discussed.

2. Experimental

Materials and Methods

The powders used in preparing the Hf-Ti-Si arc melted alloy were:

1. 49 wt % (33 at.%) $HfSi_2$ of 99.99% purity and 1-5 μm nominal particle size (Alfar Aesar, South Africa)
2. 51 wt %, (67 at.%) $TiSi_2$ of 99.95% purity and 40 μm nominal particle size (Alfar Aesar, South Africa)

Prior to arc melting the powders under a vacuum, a mixture was obtained by low speed (150 rpm) planetary ball milling (agate pot and balls) of the disilicides for 4 h in hexane, followed by drying and compaction at 100 MPa.

A bulk polyacrylonitrile-based carbon fibre cloth (Twill 2/2, 3K, 200 g/m^2 linear density, Engineered Cramer Composites, Germany) was acquired to serve as the reinforcement for the composite. To prepare the surfaces of the fibres for coating with a boron nitride precursor, they were thermally desized in a tube furnace stepped up to 1000 °C at the rate of 20 ºC/min and held for 5 minutes with flowing argon gas. The boron nitride precursor was prepared by mixing a urea-boric acid mixture (8:1 by mass respectively) in ethanol and filtering off residual crystals. The precursor covered the fibres during the solution dipping technique, before the fibres were withdrawn from the solution and dried in ambient air. The boron nitride coating for the carbon fibres was then realised by a nitriding reaction between nitrogen gas and the urea-boric acid mixture at 1000 °C for 1 h.

The BN-coated carbon fibres were infused with phenolic resin using a vacuum assisted resin infiltration facility at room temperature for 4 h. This introduced a resin matrix to the fibre cloth and was followed by curing at 100 °C for 8 h to allow crosslinking in the resin. Pyrolysing the crosslinked resin in an argon atmosphere at 1000 °C for 1 h yielded a carbon matrix. Thus, an intermediate C_f/C composite with a bulk density 1.45 g/cm^3 and open porosity of 28.3% was obtained. Discs of 20 mm nominal diameter and 3 mm thickness were cut from the intermediate composite for subsequent processing as summarised in **Figure 1**a.

2.5 g of pulverised alloy powder was placed in contact with each of the cut C_f/C composite discs in a BN lined graphite crucible. The graphite crucible was positioned inside a hollow cylindrical die and fixed in contact with a conventional graphite assembly of punches and rams in a pulsed electric current sintering (PECS) furnace illustrated in **Figure 1**b. The crucible was overlaid with graphite foils to avoid high temperature fusion with the graphite die. The whole die set-up was also covered with carbon fibre insulating cloth. The ram confining force was set at the minimum possible, 3 kN, to ensure electrical contact with the graphite crucible but avoid the use of excessive pressure. A pulsed electric current of maximum 4 kA was applied to heat the crucible at a rate of 200 °C/min to 2000 °C. This caused the alloy powder to melt and be drawn into the open pore channels of the intermediate C_f/C composite by capillary transport. As the alloy permeated the intermediate C_f/C composite, contact with the carbon matrix led to carbide formation reactions. A 30-minute hold time was used to allow the melting, permeation and

reaction processes to complete. The resulting hybrid carbide UHTC matrix composites consisted of C_f/(Hf,Ti)C-SiC, which is subsequently shortened to C_f/HTS.

Oxyacetylene (OAT) flame test

The high temperature testing of the C_f/HTS composite discs was performed for 30 seconds in air using an oxyacetylene torch flame. The sample was secured inside a graphite sample holder and fitted in water cooled graphite jacket as shown in **Figure 2**. The acetylene:oxygen gas volumetric flow ratio was 1:1.35, the distance between the torch nozzle (No.13, 1.5 mm diameter; British Oxygen Company, UK) tip and the C_f/HTS composite surface was 10 mm and the heat flux at the sample surface has been estimated at ~17 MW/m^2; details of how the latter was determined utilising a Gardon gauge-type heat flux sensor (Vatell Corp., USA) has been reported by Paul *et al.*[22]. The temperature of the surface exposed to the oxyacetylene flame was measured by non-contact methods using two systems; a 2 colour infra-red pyrometer (Marathon MR1SCSF, Raytek GmbH, Germany) and a thermal imaging camera (Thermovision A40, FLIR Systems AB, Sweden). The former was important in minimising the effect of emissivity from the phase changes on the surface of the materials. A temperature map for a sample during testing is inserted in **Figure 2**. The radiation ratio was assumed to remain constant, hence the emissivity value was kept at 1.0. Four samples of the C_f/HTS composite were tested. Dimensional changes to the tested discs were determined and the shrinkage calculated. The mass lost by the disc was determined and the mass ablation rate calculated as a ratio of the mass change to the exposure time.

Characterisation

The composites were characterised before and after OAT testing using a variety of techniques. X-ray diffraction (Bruker D2 Phaser, Bruker Corporation, USA) using a monochromatic cobalt source (λ = 1.79 eV) at 30 kV for a 2-theta range of 10-90° yielded crystallographic data. Field emission scanning electron microscopy (Zeiss Sigma Evo 60, Carl Zeiss AG, Germany) was performed in both backscattered diffraction (BSD) and secondary electrons (SE) modes to analyse the phase distributions in the microstructures of the C_f/HTS composites. The elements present were also determined using a Bruker AXS Quantax 4010 (Bruker Corporation, USA) energy dispersive spectrometry detector.

Quantitative Analysis

The distribution of phases in the back-scattered diffraction micrographs were investigated using probability-based statistical analysis. Image analysis was first performed using ImageJ software on regions of interest, measuring 40 x 50 μm, by optimised contrasting of the micrographs and thresholding into black and white domains. The porosity across the scale profile was quantitatively recorded and the pore areas fitted to a 3-parameter Weibull probability plot.

3. Results and Discussion

Virgin C_f/HTS Composite

A virgin C_f/HTS composite disc is shown in **Figure 3**a. The four dics prepared had a residual porosity of 5.6 ± 1.9%. TiC (PDF 006-0614), HfC (PDF 081-8969) and SiC (PDF 073-1665) phases were observed in the matrix as shown in **Figure 3**b. Unreacted silicides were not detected by XRD. The white phase that precipitated close to the carbon matrix/alloy interface, shown in **Figure 3**c-d, is a solid solution of carbides of Hf and Ti. The virtually uniform distribution of the carbon element in the EDS dot map in **Figure 3**d confirms the formation of the carbides in the matrix. The spatial incidence of Hf and Ti in the maps also confirms the existence of a (Hf,Ti)C solid solution (PDF 001-6522). At 2000°C a complete HfC-TiC solid solution is expected[23].

Oxidised C_f/HTS Composite Discs

An ablated C_f/HTS composite disc is shown in **Figure 4**. The mean mass ablation rate of the prepared C_f/HTS composites after exposure to the oxyacetylene flame was 0.0014 g/s. The discs showed a mean radial shrinkage of 0.57 ± 0.21% and a thickness shrinkage of 5.19 ± 2.68%. The oxidized C_f/HTS composite surfaces had a brownish colour, as shown in **Figure 4**c. The surface was characterized by transparent and solid bubbles of assorted sizes. Details concerning the formation of bubbles on the C_f/HTS composite surface are discussed in subsequent sections.

Oxidation Reactions

XRD analysis results in **Figure 5**, shows that a range of different oxides were formed in the scale, including HfO_2 (PDF 65-1142), SiO_2 (PDF 75-0923) and TiO_2 (PDF 21-1276) as shown by Equations 1-3, and ternary titanate ($HfTiO_4$, PDF 40-0794) and silicate phases ($HfSiO_4$, PDF 20-467) shown by Equations 4-5.

$$2(Hf,Ti)C + 5.5O_2 \rightarrow 2HfO_2 + 2TiO_2 + CO_2 \quad (1)$$

$$2SiC + 3.5O_2 \rightarrow 2SiO_2 + CO_2 \quad (2)$$

$$2SiC + 3.5O_2 \rightarrow 2SiO + 2CO_2 \quad (3)$$

$$HfO_2 + SiO_2 \rightarrow HfSiO_4 \quad (4)$$

$$HfO_2 + TiO_2 \rightarrow HfTiO_4 \quad (5)$$

$$TiO_2 + SiO_2 \rightarrow TiSiO_4 \quad (6)$$

Equation (6) represents the formation of $TiSiO_4$, which is so unstable that its existence is sometimes considered hypothetical[24]. No HfO_2-TiO_2-SiO_2 phase diagram was found in the literature; therefore reference to the different pseudo-binary systems of HfO_2-TiO_2, HfO_2-SiO_2 and TiO_2-SiO_2 in **Figure 6**, was necessary. Inference from the ZrO_2-TiO_2-SiO_2 phase diagram [25] was also useful as ZrO_2 and HfO_2 are isostructural[26]. No evidence for any quaternary oxide complex was observed.

The HfO_2-TiO_2-SiO_2 pseudo-ternary system, when analysed from the aforementioned pseudo-binary systems viewpoint, is somewhat complicated in that it involves:

(a) Extensive immiscibility – phase separation regions in the pseudo-binary systems at specific composition and temperature ranges, shown in **Figure 6**;
(b) Metastable phases – temperature changes lead to oxide phases passing through spinodal regions of instability;
(c) Phase transitions – oxides in the system transform in crystallographic form due to temperature changes. For example, hafnia from monocyclic to tetragonal and silica from quartz to tridymite.

The crystallographic and thermodynamic summary of the ternary compounds ($HfTiO_4$, $HfSiO_4$ and $TiSiO_4$) is presented in **Table 1**.

$HfSiO_4$ undergoes solid state decomposition into HfO_2 and SiO_2 at 2000 °C[27], as depicted in the phase diagram in **Figure 6**b. In the silica rich system, the possibility of a eutectic of $HfSiO_4$ and SiO_2 may exist for temperatures above the decomposition temperature, although Bundschuh and Schutze[28] cited a lower temperature of 1680 ± 15 °C. Since the HfO_2-SiO_2 phase diagram is only partially known, no definite temperature is given in the literature on when the solid-state dissociation occurs. In the ZrO_2-SiO_2 system, the range is generally between 1540 °C and 1700 °C, as presented by Kaiser et al.[29] who arrived at 1687 °C from thermodynamic simulations.

When cooling, HfO_2 transforms from the tetragonal phase to the monocyclic at 1570 ± 20 °C. TiO_2 is soluble in these phases to a maximum of 10 and 30 mol.% respectively[30].With a Hf concentration of 30.2 at% used in this study, the phase diagram in **Figure 6**a shows that $HfTiO_4$ will be in co-existence with TiO_2 liquid when quenched. The brownish colour observed during the OAT is a characteristic colour of liquid TiO_2. The solid solubility of HfO_2 in $HfTiO_4$ is around 10 mol% and the maximum solubility occurs at 1980 °C[30]. From the TiO_2-SiO_2 phase diagram[31] in **Figure 6**c, the 23 at.% TiO_2 used in this study is close to the eutectic of 21 wt% TiO_2 at 1540°C. TiO_2, rutile, can be a network former when interacting with silica[31]. Ferris[32] showed the thermodynamic possibility of a $ZrTiO_4$-$TiSiO_4$ solid solution, which can be extrapolated to the $HfTiO_4$-$TiSiO_4$ system.

The mutual interactions of the ternary silicates in the system have not been extensively analysed. Ramakirs and co-workers[33] showed that $HfSiO_4$–$TiSiO_4$ are completely mutually soluble and phase separation does not occur. Ferris[32] analysed the formation of a $ZrSiO_4$–$TiSiO_4$ solid solution, which can be related to the $HfSiO_4$–$TiSiO_4$ system. The solid solution formation involved the replacement of Zr by Ti in the crystal. Extension of the idea to the present study would lead to equations (7) and (8). The latter is thermodynamically preferred; Ti from the rutile is thermodynamically likely to substitute for Si rather than Hf in the crystal[32].

$$TiO_2 + HfSiO_4 \leftrightarrow TiHfO_4 + SiO_2 \quad (7)$$

$$TiO_2 + HfSiO_4 \leftrightarrow TiHfO_4 + HfO_2 \quad (8)$$

Scale Cross-sectional Profile

The cross-sectional profile of the scale is shown in **Figure 7**a. The composite formed a scale of about 52 μm thickness, which had four distinct microstructural layers shown in **Figure 7**b. The latter were analysed individually for compositional differences, and the EDS maps are shown in **Figure 7**c.

Layer 1 (scale surface)
An intra-connecting network of TiO_2-HfO_2 solid solution (bright phase) and SiO_2 (dark phase) characterises this layer; their separation is evidence of immiscibility. It is not possible, however, to draw conclusions on the mechanism underpinning the phase separation in the system simply by analysing the final microstructure; most mechanisms ultimately arrive at the same microstructure when the system is quenched[17,34]. Monaghan et al.[35] described the spinodal phase segregation as occurring spontaneously, being influenced by the bond rearrangement in the silica-rich composition. It should be noted that the solid-state decomposition occurs at a temperature very slightly above the eutectic melting points of the two liquids, TiO_2 and HfO_2.

Layer 2
Discrete spherical HfO_2 crystallites were observed to be embedded in a continuous SiO_2-rich matrix. The HfO_2 and SiO_2 phases will have formed from the solid decomposition of the $HfSiO_4$, which was observed from the XRD analysis and is also in agreement with the phase diagram. As no solid solution is formed in the system, this led to the existence of the discrete spheres of HfO_2 in SiO_2. It is therefore believed that the HfO_2 crystallized out of the silica matrix.

The possibility of the formation of metastable compounds such as $HfSiO_6$ exists, being projected from the $ZrSiO_6$ indicated by Kaiser[29] as part of the solid state decomposition reactions. Solid SiO_2 forms from the decomposition and is immediately dissolved in the liquid phase as shown in the phase diagram in **Figure 6**. Verdon et al.[17] indicated the formation of a $Hf_xSi_yO_z$ compound in an oxidised HfC-SiC coating. Although the exact identity was not investigated, the compound provided oxidation protection to the C/C system underneath the coating. In the case of $HfSiO_4$ co-exising with $ZrSiO_4$, for which the Zr may be related to the Ti in the present study, Cota et al.[36] showed that the compound $Zr_{1-x}Hf_xSiO_4$ was formed from solution when the composition was equimolar, i.e. $x = 0.5$. The oxidation resistance of $Zr_{1-x}Hf_xSiO_4$ has not been recorded in the literature.

Layer 3
Microstructural analysis showed the formation of dendritic clusters or "corals" of TiO_2, possibly $TiSiO_4$, in co-existence with SiO_2 and SiC. In layers 3 and 4, the virgin SiC detected was confirmed by XRD analysis. Dendrites are believed to have crystallized in the HfO_2-depleted matrix at a temperature lower than the melting point of SiO_2. The coral microstructure in Layer 3 is attributed to the coalescence and growth of the TiO_2-rich precipitates.

Layer 4 (scale base)
Layer 4 is the scale/virgin material interface, evidenced by the upper band that is oxygen rich and the lower band that is silicon rich. This suggests that the silica-depleted region is located above the scale/virgin material interface, the lower region being SiC. The co-existence of Hf and

Ti in the oxygen-rich band is marked, also suggesting that the $HfTiO_4$ phase dominates the dendritic "corals". Moreover, regions of phase separation similar to those that dominate Layer 1 were identified. HfC, TiC and SiC are all capable of reacting with their oxides, the point at which chemical equilibrium is achieved being determined by the partial pressures of the exiting CO and CO_2 formed in relation to the ingressing O_2 partial pressure. The oxidation of the reinforcing carbon fibres according to Equations 9-10 also contributes to the CO and CO_2 in the system. The details of the oxidation and degradation of the reinforcing fibres in the C_f/HTS composite, mostly located in areas where the scale was denuded off the surface (not shown), is the subject of a different paper (to be published) that deals with related reinforcement in other UHTC composites.

$$C + O_2 \rightarrow CO_2 \qquad (9)$$

$$2C + 2O_2 \rightarrow 2CO_2 \qquad (10)$$

Porosity in the Scale

The pore size distribution in the four layers of the scale was compared by the 3-parameter Weibull plot based on individual pore areas, as illustrated in **Figure 8**. Layer 1 is characterised the largest pores in the scale, of up to ~30 μm^2. Conversely, layer 2 has the finest pores, with about 30% having an area of <0.1 μm^2 and a total of 80% with less than 1 μm^2 area. Layer 2 also has the least number of pores.

The highest number of pores was located in layer 3; both layers 3 and 4 had about ten times the number of pores found in Region 2. Layer 3 was the hafnia deficient layer in the scale, whereas layers 1 and 2 were silica rich. Layer 4 was the scale/virgin material interface and was characterised by relatively limited oxides of Si, Ti and Hf; carbide phases were present. The number of pores in layer 4 suggests that the carbides were oxidized and formed gaseous oxides of carbon, Equations (1)-(3), which formed pores in attempting to escape. The limited presence of silica could also have led to the inadequate filling of the pores by molten silica.

It is plausible that the oxide gases intumesced through the scale towards the surface but were impeded by a higher liquid viscosity in layer 1 and thus formed glassy bubbles in this layer, as shown in **Figure 8**. In some areas transparent bubbles were observed at the surface, as shown in the **Figure 8**c insert, probably due to the vapour pressure of the escaping gases being sufficient to "blow" through the SiO_2-rich surface. The total partial pressures of the gases in contact with the scale determine whether the latter will rupture or remain intact. The quantitative consideration of the total partial pressures of the escaping gases ($P_{CO} + P_{CO2}$) compared with that of the scale formed gives an indication of whether the scale was capable of protecting the matrix from oxidation, as presented by Hale[37]. The following rule of thumb applies[37]:

$PCO + PCO_2 < 1$ the scale is stable and hence protective
$PCO + PCO_2 > 1$ the scale is unstable and hence unprotective

The presence of very large pores just beneath the exposed surface of the scale, layer 1, can be related to the observation of the glassy bubbles on the surface in **Figure 8**b and c. The absence

of ruptured bubbles on the surface indicates that layer 1 is a protective shield over the rest of the scale, whilst the overall scale adhered to the virgin bulk composite.

A schematic of the scale top layer, which was characterised by phase separation and surface bubbles under which large pores were observed, is illustrated in **Figure 8**. The resistance of the layer to rupturing, especially at the bubble sites, shows that the phase immiscibility contributed positively to the ablation resistance of the scale formed.

4. Conclusion

Exposure of the carbon fibre reinforced (Hf,TiC)-SiC matrix resulted in the formation of a multi-layered scale. The C_f/HTS composite showed an average mass ablation rate of 0.0014 g/s after exposure to a heat flux of ~17 MW/cm^2 during oxyacetylene torch testing for 30 s. The multicomponent scale consisted of oxides of Hf, Ti and Si, as well as $HfTiO_4$ and $HfSiO_4$. An intra-connecting network of TiO_2, $HfTiO_4$ and SiO_2 dominated the outermost layer of the scale, which underwent phase separation. The scale layer closest to the scale/virgin material interface showed the formation of dendritic "corals" of $HfTiO_4$ in a SiO_2 depleted band. Oxidation reactions led to the production of gaseous products that are believed to have intumesced through the scale to form bubbles at the surface. The largest pores in the scale and surface bubbles that resisted rupture were the dominant features of the outermost phase-separated layer. Phase separation in the scale top layer, which was silica-rich, led to improved resistance to scale rupture.

5. Funding

This work was funded by the DST-NRF Centre of Excellence in Strong Materials (CoE-SM). Opinions expressed and conclusions arrived at, are those of the authors and are not necessarily to be attributed to the CoE-SM.

6. Acknowledgements

The authors are grateful to Dr. Virtudes Rubio Diaz and Matthew Porter for running the oxyacetylene torch tests at the University of Birmingham.

7. References

1. Glass, D. Physical Challenges and Limitations Confronting the Use of UHTCs on Hypersonic Vehicles. *17th AIAA Int. Sp. Planes Hypersonic Syst. Technol. Conf.* 1–25 (2011).

2. Glass, D. E., Merski, N. R. & Glass, C. E. Airframe Research and Technology for Hypersonic Airbreathing Vehicles. in *11th AIAA Int. Sp. Planes Hypersonic Syst. Technol. Conf.* 5137 (2002).

3. Backman, L. & Opila, E. J. Thermodynamic assessment of the group IV, V and VI oxides for the design of oxidation resistant multi-principal component materials. *J. Eur. Ceram. Soc.* **39**, 1796–1802 (2019).

4. Monteverde, F. & Bellosi, A. Development and characterization of metal-diboride-based composites toughened with ultra-fine SiC particulates. *Solid State Sci.* **7**, 622–630 (2005).

5. Fahrenholtz, W. G., Hilmas, G. E., Talmy, I. G. & Zaykoski, J. A. Refractory diborides of zirconium and hafnium. *J. Am. Ceram. Soc.* **90**, 1347–1364 (2007)..

6. Opila, E., Levine, S. & Lorincz, J. Oxidation of ZrB_2- and HfB_2-based ultra-high temperature ceramics: Effect of Ta additions. *Journal of Materials Science* **39**, 5969–5977 (2004).

7. Poerschke, D. L., Novak, M. D., Abdul-Jabbar, N., Krämer, S. & Levi, C. G. Selective active oxidation in hafnium boride-silicon carbide composites above 2000°C. *J. Eur. Ceram. Soc.* **36**, 3697–3707 (2016).

8. Fahrenholtz, W. G. & Hilmas, G. E. Oxidation of ultra-high temperature transition metal diboride ceramics. *Int. Mater. Rev.* **57**, 61–72 (2012).

9. Gasch, M., Ellerby, D., Irby, E., Beckman, S., Gusman, M. and Johnson, S. Processing, properties and arc jet oxidation of hafnium diboride/silicon carbide ultra high temperature ceramics. *J. Mater. Sci.* **39**, 5925–5937 (2004).

10. Talmy, I.G., Zaykoski, J.A. and Opeka, M.M. High Temperature Chemistry and Oxidation of ZrB_2 Ceramics Containing SiC, Si_3N_4, Ta_5Si_3, and $TaSi_2$. *J. Am. Ceram. Soc.* **91**, 2250–2257 (2008).

11. Di Maso, A., Savino, R., Fumo, M. S., Silvestroni, L. & Sciti, D. Arc-Jet Testing on HfB_2-$TaSi_2$ Models: Effect of the Geometry on the Aerothermal Behaviour. *Open Aerosp. Eng. J.* **3**, 10–19 (2010).

12. Zou, J., Rubio, V. & Binner, J. Thermoablative resistance of ZrB_2-SiC-WC ceramics at 2400°C. *Acta Mater.* **133**, 293–302 (2017).

13. Carney, C. M., Parthasarathy, T. A. & Cinibulk, M. K. Oxidation resistance of hafnium diboride ceramics with additions of silicon carbide and tungsten boride or tungsten carbide. *J. Am. Ceram. Soc.* **94**, 2600–2607 (2011).

14. Savino, R., De Stefano Fumo, M., Paterna, D., Di Maso, A. & Monteverde, F. Arc-jet testing of ultra-high-temperature-ceramics. *Aerosp. Sci. Technol.* **14**, 178–187 (2010).

15. Jayaseelan, D. D., Zapata-Solvas, E., Brown, P. & Lee, W. E. In situ formation of oxidation resistant refractory coatings on SiC-reinforced ZrB_2 ultra high temperature ceramics. *J. Am. Ceram. Soc.* **95**, 1247–1254 (2012).

16. Karlsdottir, S. N. & Halloran, J. W. Formation of oxide films on ZrB_2–15 vol% SiC composites during oxidation: evolution with time and temperature. *J. Am. Ceram. Soc.* **92**, 1328–1332 (2009).

17. Verdon, C., Szwedek, O., Allemand, A., Jacques, S., Le Petitcorps, Y. and David, P. High temperature oxidation of two- and three-dimensional hafnium carbide and silicon carbide coatings. *J. Eur. Ceram. Soc.* **34**, 879–887 (2014).

18. Makurunje, P., Monteverde, F. & Sigalas, I. Self-generating oxidation protective high-temperature glass-ceramic coatings for C_f/C-SiC-TiC-TaC UHTC matrix composites. *J. Eur. Ceram. Soc.* **37**, 3227–3239 (2017).

19. Rao, C. N. R., Vanitha, P. V & Cheetham, A. K. Phase Separation in Metal Oxides. *Chem. Eur. J.* **9**, 828–836 (2003).

20. Hudon, P. & Baker, D. R. The nature of phase separation in binary oxide melts and glasses. II. Selective solution mechanism. *J. Non. Cryst. Solids* **303**, 346–353 (2002).

21. Hudon, P. & Baker, D. R. The nature of phase separation in binary oxide melts and glasses. II. Selective solution mechanism. *J. Non. Cryst. Solids* **303**, 346–353 (2002).

21. Hudon, P. & Baker, D. R. The nature of phase separation in binary oxide melts and glasses I: Silicate systems. *J. Non. Cryst. Solids* **303**, 299–345 (2002).

22. Paul, A., Binner, J. G. P., Vaidhyanathan, B., Heaton, A. C. J. & Brown, P. M. Heat flux mapping of oxyacetylene flames and their use to characterise C_f-HfB_2 composites. *Adv. Appl. Ceram.* **115**, 158–165 (2016).

23. Rogl, P., Naik, S. K. & Rudy, E. A constitutional diagram of the system TiC-HfC-WC. *Monatshefte für Chemie* **108**, 1325–1337 (1977).

24. Rignanese, G. M., Rocquefelte, X., Gonze, X. & Pasquarello, A. Titanium oxides and silicates as high-κ dielectrics: A first-principles investigation. *Int. J. Quantum Chem.* **101**, 793–801 (2005).

25. Wannagon, A., Mishima, N., Wakasugi, T., Ota, R. & Fukunaga, J. Formation and thermal stability of gels in the SiO_2-TiO_2-ZrO_2 system. *J. Ceram. Soc. Japan* **105**, 940–946 (1997).

26. Stemmer, S., Chen, Z., Levi, C.G., Lysaght, P.S., Foran, B., Gisby, J.A. and Taylor, J.R. Application of metastable phase diagrams to silicate thin films for alternative gate dielectrics. *Japanese J. Appl. Physics, Part 1 Regul. Pap. Short Notes Rev. Pap.* **42**, 3593–3597 (2003).

27. Criscione, J. . M., Mercuri, R. A., Schram, E. P., Smith, A. W. & Volk, H. F. *High temperature protective coatings for graphite*. Union Carbide Corp., Parma, Ohio (1964).

28. Bundschuh, K. & Schütze, M. Materials for temperatures above 1500˚C in oxidizing atmospheres Part I : Basic considerations on materials selection. *Mater. Corros.* **52**, 204–212 (2001).

29. Kaiser, A., Lobert, M. & Telle, R. Thermal stability of zircon (ZrSiO4). *J. Eur. Ceram. Soc.* **28**, 2199–2211 (2008).

30. Coutures, J. P. & Coutures, J. The System HfO_2-TiO_2. *J. Am. Ceram. Soc.* **70**, 383–387 (1987).

31. Ricker, R. W. & Hummel, F. A. Reactions in the System TiO_2-SiO_2; Revision of the Phase Diagram. *J. Am. Ceram. Soc.* **34**, 271–279 (1951).

32. Ferriss, E. D. A. Corrosion of UO_2 and thermodynamic properties of solid solutions in the zircon group. Doctoral Thesis (The University of Michigan, 2009).

33. Ramakrishnan, S. S., Gokhale, K. V. G. K. & Subbarao, E. C. Solid solubility in the system zircon-hafnon. *Mater. Res. Bull.* **4**, 323–327 (1969).

34. Block, S. & Levin, E. M. Structural interpretation of immiscibility in oxide systems: II, Coordination principles applied to immiscibility. *J. Am. Ceram. Soc.* **40**, 113–118 (1957).

35. Monaghan, S., Greer, J. C. & Elliott, S. D. Thermal decomposition mechanisms of hafnium and zirconium silicates at the atomic scale. *J. Appl. Phys.* **97**, 114911 (2005).

36. Cota, A., Burton, B.P., Chaín, P., Pavón, E. and Alba, M. D. Solution Properties of the System $ZrSiO_4$−$HfSiO_4$: A Computational and Experimental Study. *J. Phys. Chem. C* **117**, 10013–10019 (2013).

37. Hale, D. V, Hoover, M. J. & O'Neill, M. J. Phase Change Materials Handbook, NASA CR-61363. *NASA Contract. Rep.* 232 (1971).

38. Nishiyama, A. Hafnium-Based Gate Dielectric Materials. in *High Permittivity Gate Dielectric Materials,* 153–181 (Springer, 2013).

39. Jain, A., Ong, S.P., Hautier, G., Chen, W., Richards, W.D., Dacek, S., Cholia, S., Gunter, D., Skinner, D., Ceder, G. and Persson, K.A. The Materials Project: A materials genome approach to accelerating materials innovation. *APL Mater.* **1**, 011002 (2013).

40. Alexanderspeer, J. & Cooper, B. J. Crystal structure of synthetic hafnon, $HfSiO_4$, comparison with zircon and the actinide orthosilicates. *Am. Miner.* **67**, 804–808 (1982)..

41. Newton, R. C., Anning, C. E. M., Anchar, J. M. H. & Olasanti, C. V. C. Free energy of formation of zircon based on solubility measurements at high temperature and pressure. *Am. Mineral.* **95**, 52–58 (2010).

42. Plane, J. M. C. On the nucleation of dust in oxygen-rich stellar outflows. *Phil. Trans. R. Soc.* **371**, 20120335 (2013).

43. Varghese, J., Joseph, T., & Sebastian, M. T. Sol-gel derived $TiSiO_4$ ceramics for high-k gate dielectric applications. *AIP Conf. Proc.* **1372**, 193–197 (2011).

44. Seriani, N., Pinilla, C., Cereda, S., De Vita, A. & Scandolo, S. Titania-silica interfaces. *J. Phys. Chem. C* **116**, 11062–11067 (2012).

List of Figure Captions

Figure 1: (a) Summary of steps used in preparing the C_f/HTS composite, (b) a schematic of the graphite crucible fixed inside the die and secured by assembles of punches and rams in the pulsed electric current sintering (PECS) furnace.

Figure 2: Photograph of a C_f/HTS composite disc in a graphite sample holder during the oxyacetylene torch flame test. Insert shows the related temperature mapping photograph.

Figure 3: (a) Virgin C_f/HTS composite disc in the sample holder. (b) X-Ray diffractogram of the virgin C_f/HTS composite. (c) Cross-sectional microstructure of the virgin C_f/HTS composite. (d) Higher magnification SEM micrograph of the virgin C_f/HTS composite and associated elemental dot maps of C, Hf, Ti and Si.

Figure 4: (a) C_f/HTS composite disc in the sample holder (post OAT) with bubbles formed on the surface; a glassy ridge at the disc edge and a glassy deposit on the sample holder are visible. (b) Side view thermal photograph of the fluid loss during torch testing of the C_f/HTS disc. (c) The two distinct regions of the bright-white melt at the centre of the disc and brownish melt at the peripheries of the disc. (d) Temperature-time profile measured at the centre of the disc.

Figure 5: X-Ray diffractogram of an oxidised C_f/HTS composite (all the samples yielded similar results).

Figure 6: Pseudo-binary phase diagrams for (a) HfO_2-TiO_2[30] (partial), (b) HfO_2-SiO_2[38] and (c) TiO_2-SiO_2[31] (partial).

Figure 7: (a) The cross-sectional back scattered electron micrograph of the scale formed on the oxidised C_f/HTS disc composite. (b) Higher magnification micrographs of the four layers (1-4) of the scale. (c) EDS dot maps of the four layers (1-4) of the scale.

Figure 8: (a) 3-Parameter Weibull plot of the pore area distributions in each of the four regions 1-4 across the scale of the oxidised C_f/HTS composite. (b) Secondary electron angular-view micrograph of the bubbles formed in the surface layer (layer 1). (c) Backscattered top-view micrograph of the bubbles formed in the surface layer (layer 1). X = base of bubble and Y is the bubble.

Figure 9: Schematic of the relationship between pores in layer 1 of the scale and the scale surface characterised by bubbles.

List of Figures

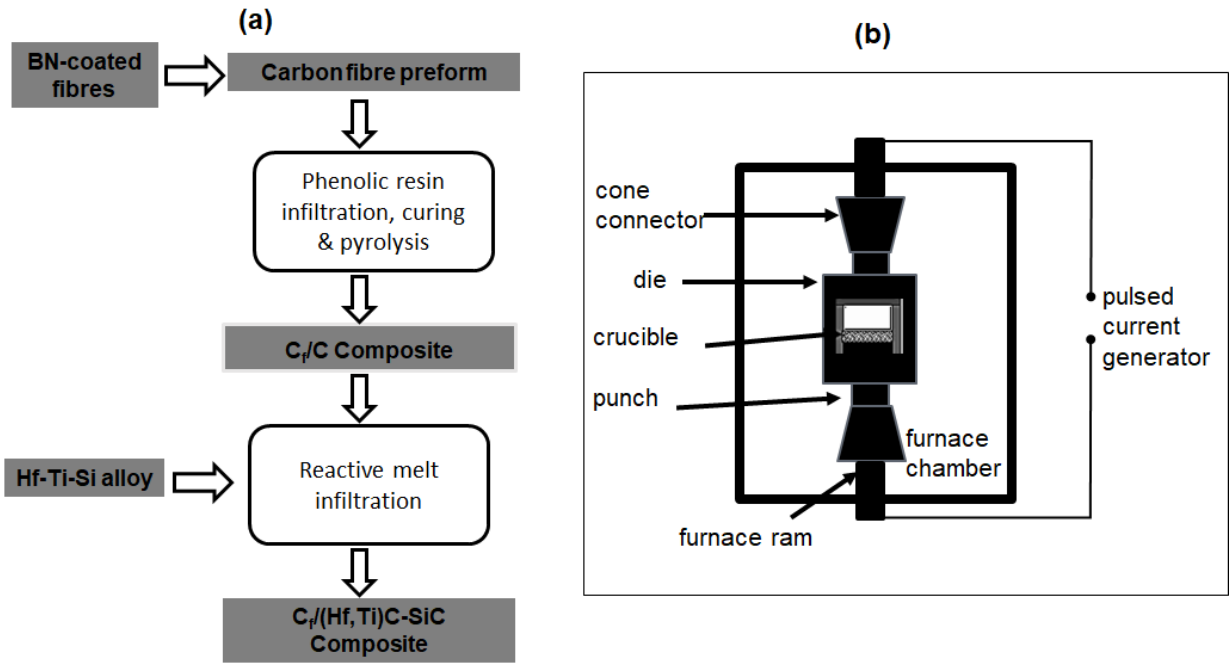

Figure 1

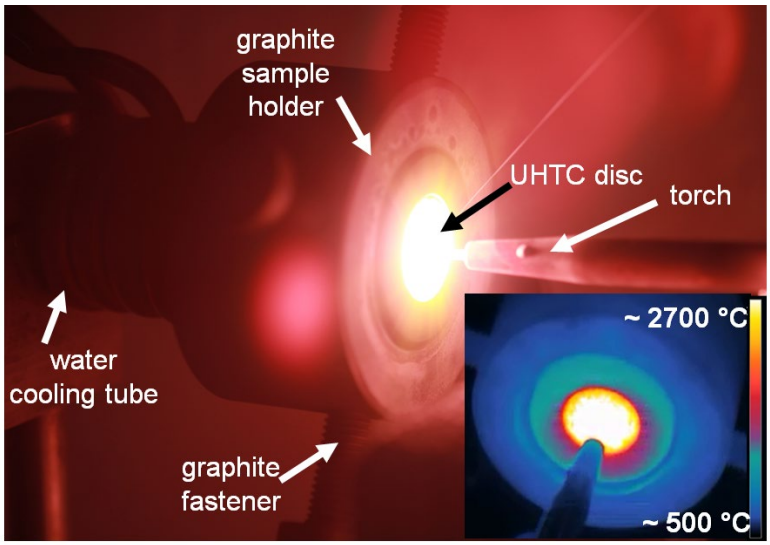

Figure 2

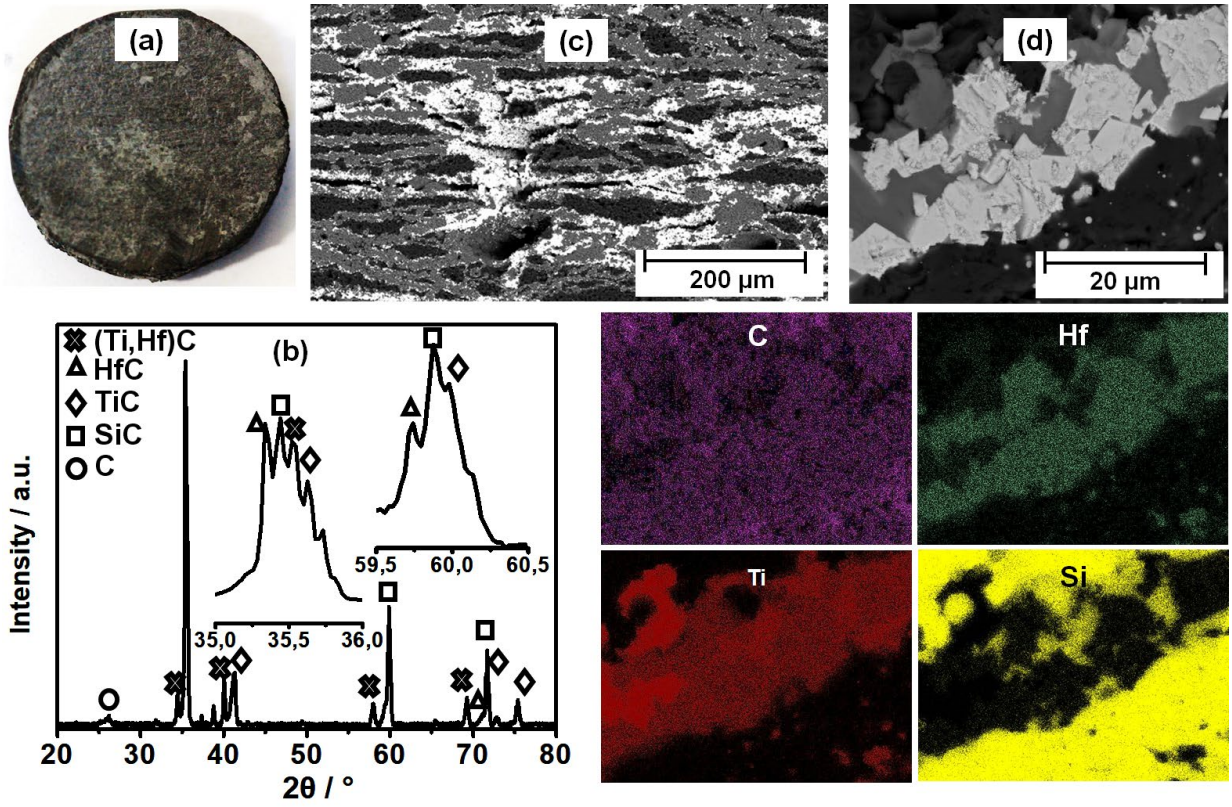

Figure 3

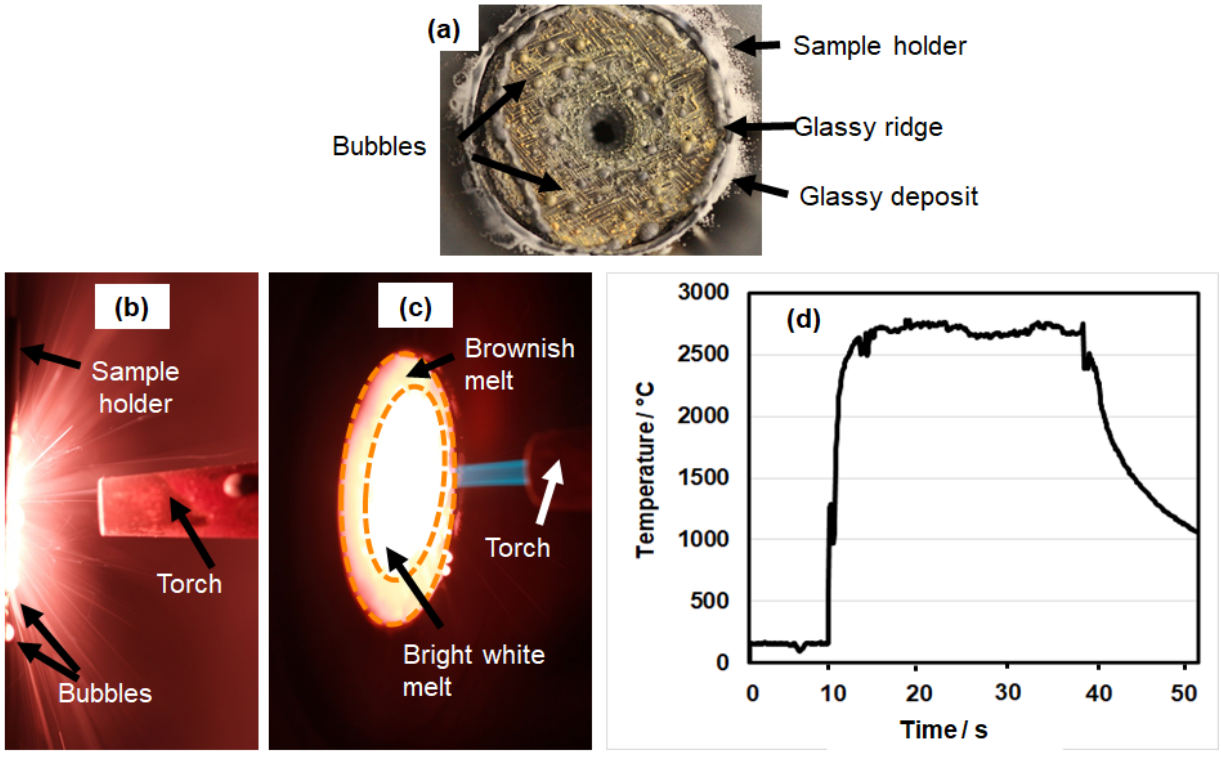

Figure 4

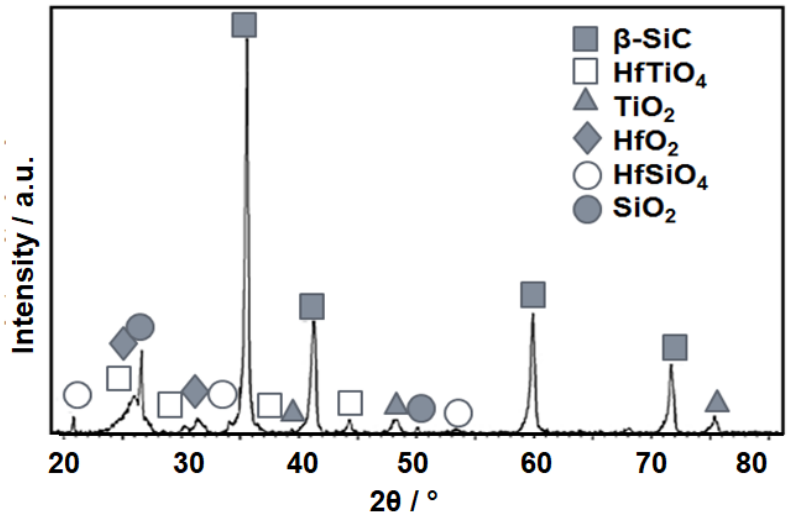

Figure 5

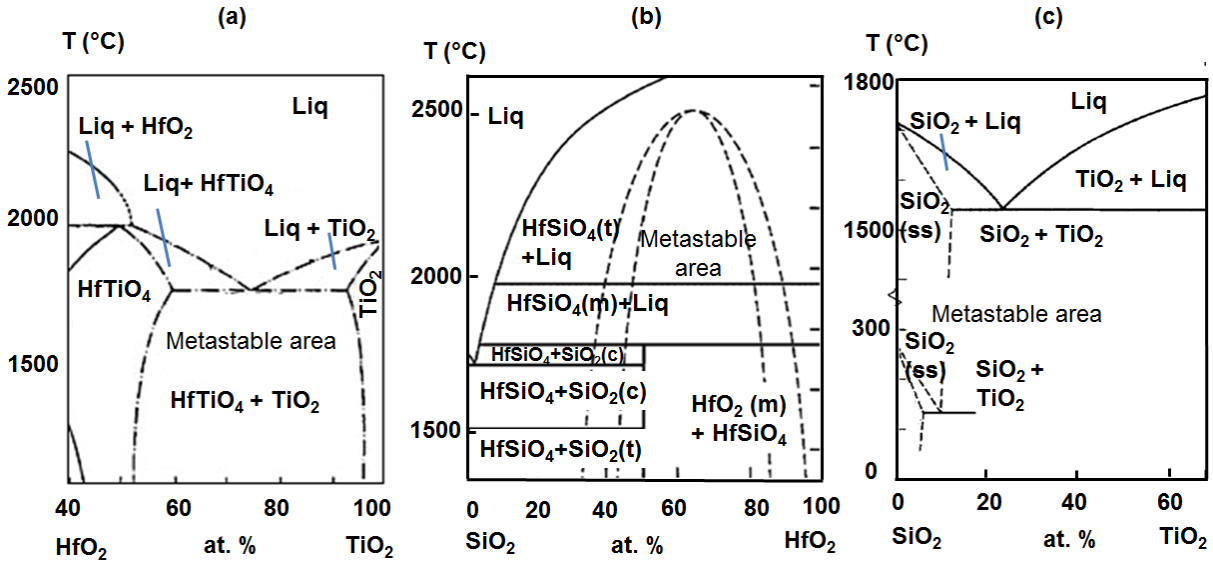

Figure 6

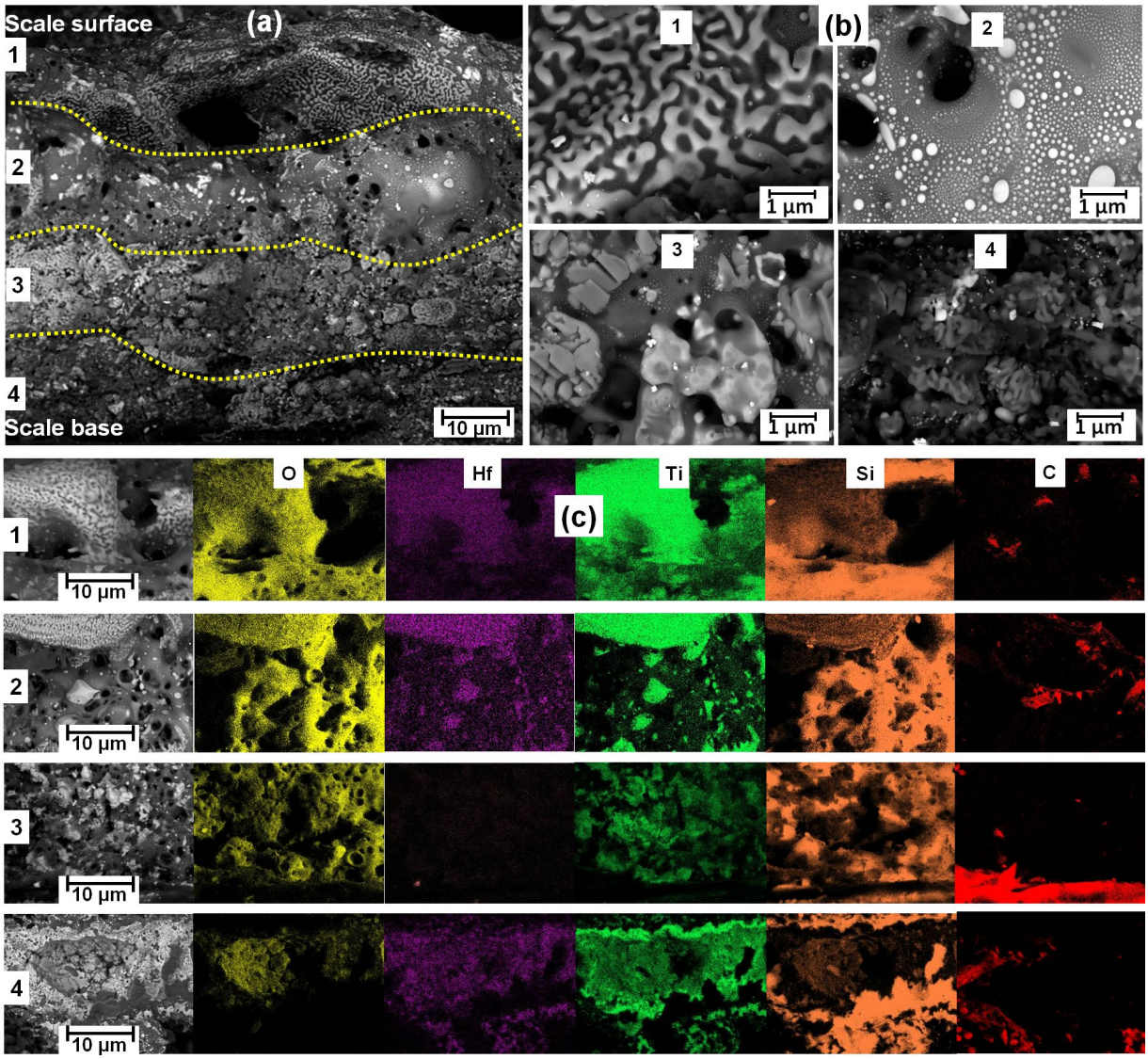
Scale surface
(a)
1
2
3
4
Scale base
10 μm
1
(b)
2
1 μm
3
4
1 μm
1 μm
1 μm
O
Hf
Ti
Si
C
(c)
1
2
3
4
10 μm
10 μm
10 μm
10 μm

Figure 7

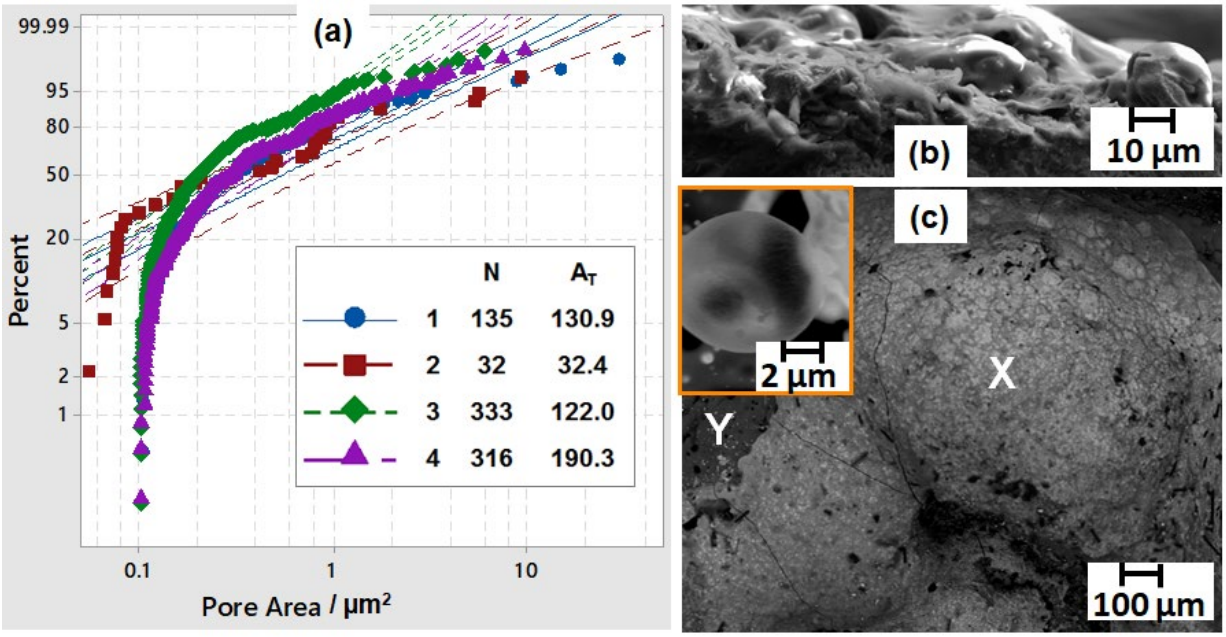

Figure 8

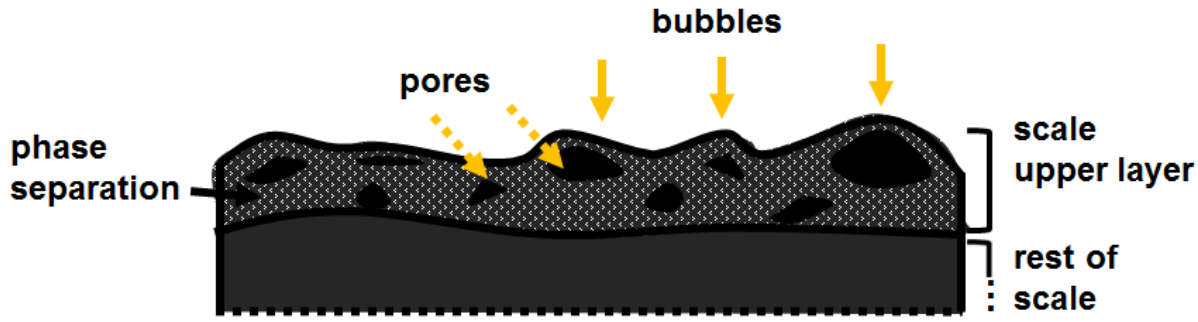

Figure 9

List of Table Captions

Table 1: Crystal and thermodynamic properties of $HfTiO_4$, $HfSiO_4$ and $TiSiO_4$.

List of Tables

Table 1

Compound	Crystal structure	Formation energy / eV	Enthalpy of formation from oxides* / kJ/mol	Gibbs energies of formation from oxides* / kJ/mol	Comments
$HfTiO_4$	triclinic (P1) a = 4.771 b = 5.685 c = 10.175 volume = 275.919[39]	-3.744[39]	ΔH°_{298K} = 20.54 ΔH°_{1800K} = 11.37	ΔG°_{298K} = 15.85 ΔG°_{1800K} = −6.74	
$HfSiO_4$	tetragonal zircon structure, ($I4_1/amd$) a = 6.625 b = 6.625 c = 6.007[39] volume = 131.816[39]	-3.674[39]	$\Delta H_{f^\circ 298K}$ = 24.98 ± 0.2[40]	ΔG°_{1050K} = 14.5[41]	Formed at 1673°C (derived from zircon system)[29] Calculated by an approximation of the Gibbs free energy of formation for zircon by the relation [40] $\Delta G = 39090 + 20.173\ T$ $(1430 \leq T \leq 2000\ K)$[40]
$TiSiO_4$	zircon structure ($I4_1/amd$) a = 6.21 b = 5.81[24] volume = 112.03[24]	-2.981[39]	$\Delta H_{f^\circ 298K}$ = -480.0[42]	Not found	Formed at 1275°C[43] although regarded as an unstable compound Phase separation occurs at temperatures greater than 600°C[44]

*Formation from the respective oxides (XO_2 and YO_2)